Applied Physics Express



LETTERS

# Large perpendicular magnetic anisotropy in epitaxial Fe/$MgAl_2O_4$(001) heterostructures

Applied Physics Express **11**, 063008 (2018)
https://doi.org/**10.7567/APEX.11.063008**

# Large perpendicular magnetic anisotropy in epitaxial Fe/$MgAl_2O_4$(001) heterostructures

Qingyi Xiang[1,2*], Ruma Mandal[2], Hiroaki Sukegawa[2], Yukiko K. Takahashi[2], and Seiji Mitani[1,2*]

[1]*Graduate School of Pure and Applied Sciences, University of Tsukuba, Tsukuba, Ibaraki 305-8577, Japan*
[2]*National Institute for Materials Science, Tsukuba, Ibaraki 305-8577, Japan*

*E-mail: xiang.qingyi@nims.go.jp; mitani.seiji@nims.go.jp

Received April 18, 2018; accepted May 12, 2018; published online June 1, 2018

We investigated the perpendicular magnetic anisotropy (PMA) and related properties of epitaxial Fe (0.7 nm)/$MgAl_2O_4$(001) heterostructures prepared by electron beam evaporation. Using an optimized structure, we obtained a large PMA energy of ~1 MJ/m$^3$ at room temperature, which is comparable to that in ultrathin-Fe/MgO(001) heterostructures. Both the PMA energy and saturation magnetization showed a weak temperature dependence, ensuring a wide working temperature range in applications. The effective magnetic damping constant of the 0.7 nm Fe layer was found to be ~0.02 using the time-resolved magneto-optical Kerr effect. This study demonstrated the suitability of the Fe/$MgAl_2O_4$ heterostructure for use in perpendicular magnetic tunnel junctions, as well as good agreement with theoretical predictions.


$MgAl_2O_4$ is considered a promising alternative to MgO for use as a barrier material in magnetic tunnel junctions (MTJs) owing to its tunable lattice constant[1,2] and preferential $\Delta_1$ band transport due to the coherent tunneling effect.[3–6] In particular, a large tunnel magnetoresistance (TMR) ratio[2,7] and improved bias dependence of the TMR ratio[1,8] have been reported in $MgAl_2O_4$-based MTJs. In addition to these TMR properties, interface-induced perpendicular magnetic anisotropy (PMA) at a $MgAl_2O_4$ interface is a crucial property for applications of perpendicularly magnetized MTJs (p-MTJs). The utilization of perpendicularly magnetized films with a large PMA energy can substantially improve the thermal stability of p-MTJs to ensure long data retention for next-generation high-density nonvolatile magnetic memories such as spin-transfer-torque magnetoresistive random access memory (MRAM) and magnetoelectric RAM.[9–19] To date, the largest interface PMA energy density of approximately 1.4 MJ/m$^3$ has been reported in an epitaxial ultrathin-Fe/MgO(001) heterostructure.[20] For $MgAl_2O_4$-based epitaxial structures, a smaller PMA energy density of ~0.4 MJ/m$^3$ has been experimentally reported in Fe/$MgAl_2O_4$(001)[21] and $Co_2FeAl$/$MgAl_2O_4$(001) heterostructures,[22] where the $MgAl_2O_4$ layers were prepared by post-oxidization of a Mg–Al metallic layer. On the other hand, according to a recent theoretical calculation,[23] an areal PMA energy density of ~1.3 mJ/m$^2$ was predicted at an Fe/$MgAl_2O_4$(001) interface, which is nearly comparable to that at an Fe/MgO(001) interface (~1.5–1.7 mJ/m$^2$). Interestingly, even the small difference in PMA density between Fe/$MgAl_2O_4$ and Fe/MgO was clearly interpreted using the second perturbation theory with the orbital-resolved densities of states. Therefore, further improvement in the PMA energy of ultrathin-Fe/$MgAl_2O_4$(001) interfaces, that is, observation of an intrinsically large PMA, is expected if a clean interface is obtained by suppressing atomic intermixing and overoxidation by process optimization. In addition, related magnetic properties of the PMA heterostructures such as magnetic damping and the temperature dependence of the PMA properties should be evaluated. The former determines the switching speed and current density in MRAM operation, and the latter determines the operating temperature range of p-MTJs.[24,25]

In this study, we investigated the magnetic properties of ultrathin-Fe/$MgAl_2O_4$ structures that were fabricated using an electron beam (EB) evaporation technique to obtain a large interface PMA. Careful tuning of the film thickness and post-annealing temperature yielded an optimized Fe (0.7 nm)/$MgAl_2O_4$ interface that showed a large PMA energy of up to ~1.0 MJ/m$^3$, which is comparable to the reported value for an Fe (0.7 nm)/MgO interface (~1.4 MJ/m$^3$).[20] We also found that the PMA energy and saturation magnetization ($M_s$) were not very sensitive to the measurement temperature. The effective damping constant was also evaluated to be ~0.02 by measuring the time-resolved magneto-optical Kerr effect (TR-MOKE) under high magnetic fields.

Figure 1(a) shows a schematic design of the multilayer structure used to examine the PMA properties at an Fe/$MgAl_2O_4$ interface. A fully epitaxial stack of MgO (5 nm)/Cr (30 nm)/Fe ($t_{Fe}$ = 0.7 nm)/$MgAl_2O_4$ ($t_{MAO}$ = 2 and 3 nm) was deposited on a MgO(001) substrate by EB evaporation (base pressure ~$1 \times 10^{-8}$ Pa). Before deposition, the substrate was annealed at 800 °C to clean its surface, and then the 5 nm MgO seed layer was deposited at 450 °C. The Cr buffer layer was deposited at 150 °C and then post-annealed at 800 °C to obtain a flat Cr(001) surface. This post-annealing temperature is critical to obtaining a large PMA for an ultrathin Fe layer deposited on a Cr buffer.[20] Temperatures of 150 and 250 °C were used for growth and post-annealing, respectively, of the ultrathin Fe to improve the surface flatness. Then, the $MgAl_2O_4$ barrier layer was deposited at 150 °C at a ~0.01 nm/s deposition rate from a high-density (98.6% of the theoretical density) sintered $MgAl_2O_4$ chip (Ube Material Industries), instead of from a $MgAl_2O_4$ substrate as in a previous report.[26] Although the barrier composition may have deviated slightly from $MgAl_2O_4$ during deposition,[26] in this study the notation "$MgAl_2O_4$" is used for simplicity. The deposited $MgAl_2O_4$ barrier was post-annealed at different temperatures (350, 400, 450, and 500 °C) to modify the Fe/$MgAl_2O_4$ interface conditions. Finally, a 2-nm-thick Ru capping layer was sputter-deposited at room temperature (RT). Throughout the growth process, the surface structures and epitaxial growth were monitored in situ by reflection high-energy electron diffraction (RHEED). The magnetic hysteresis ($M$–$H$) loops of the samples were measured using a vibrating sample magnetometer (VSM) at RT and a VSM incorporated into a superconducting quantum interference device at temperatures between 100 and 300 K. The ultrafast

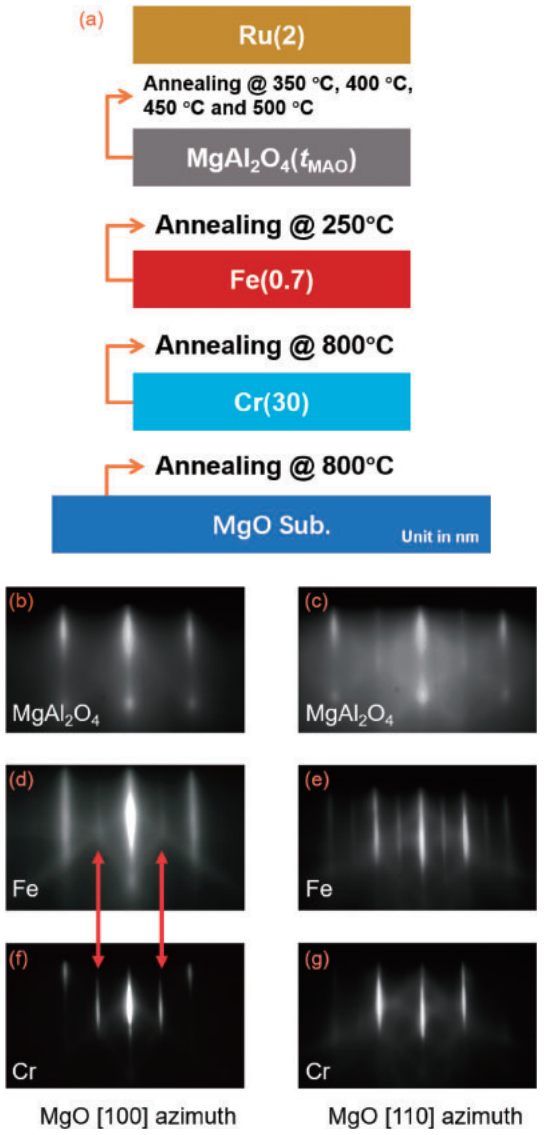


**Fig. 1.** (a) Schematic illustration of an epitaxial heterostructure. (b)–(g) RHEED patterns taken from Fe (0.7 nm)/$MgAl_2O_4$ (3 nm) sample annealed at 400 °C; incident electron beams are along the (b), (d), and (f) [100] azimuth and (c), (e), and (g) [110] azimuth of the MgO(001) substrate. Substreaks, indicated by red arrows, correspond to c(2 × 2) surface structure.

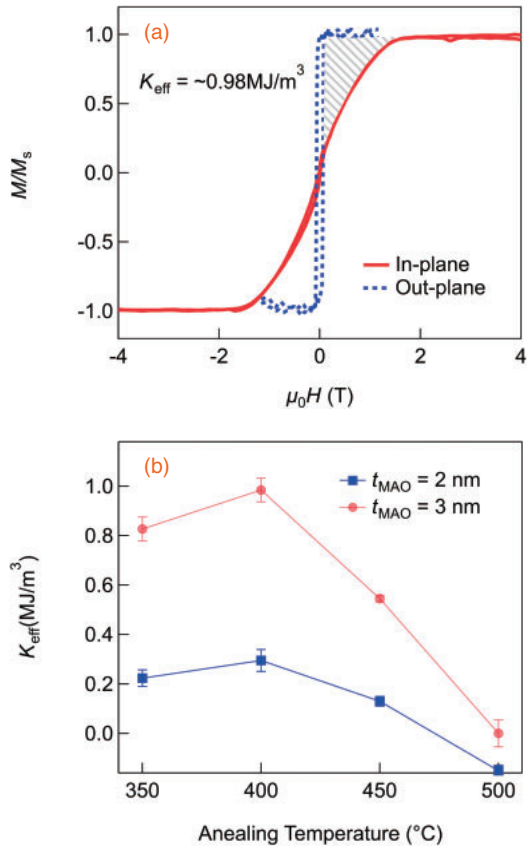


**Fig. 2.** (a) *M*–*H* loops at RT for Fe (0.7 nm)/$MgAl_2O_4$ (3 nm) sample annealed at 400 °C. Shaded area indicates the effective PMA energy density ($K_{eff}$). Positive $K_{eff}$ indicates PMA. (b) Annealing temperature dependence of $K_{eff}$ for Fe (0.7 nm)/$MgAl_2O_4$ (2 or 3 nm).

magnetization dynamics was measured by an all-optical TR-MOKE microscope to evaluate the magnetic damping. A femtosecond laser pulse at the fundamental wavelength of 1028 nm was used to excite the sample, whereas the second harmonic (wavelength, $\lambda = 515$ nm) of the fundamental beam was used to probe the magnetization dynamics by measuring the change in the Kerr rotation as a function of the time delay between the pump and probe beams. A variable magnetic field was applied at an angle of 70° with respect to the direction perpendicular to the sample surface.

The RHEED patterns of the Fe (0.7 nm)/$MgAl_2O_4$ (3 nm) sample are shown in Figs. 1(b)–1(g). As seen in Figs. 1(d) and 1(f), additional substreaks, indicated by red arrows, represent the formation of the c(2 × 2) reconstructed surface of Cr and Fe, which is believed to improve the surface flatness and consequently the magnitude of the PMA of the ultrathin Fe layer when it is capped with MgO.[20] Note that the absence of the c(2 × 2) structure for Fe was reported in Ref. 18, which differs from the present study. Further, as shown in Figs. 1(b) and 1(c), the RHEED patterns of the $MgAl_2O_4$ surface after post-annealing at 400 °C are similar to those of sputter-deposited $MgAl_2O_4$ on a thick Fe layer.[8] Therefore, the growth of a fully epitaxial structure with (001) orientation was confirmed. The patterns of the $MgAl_2O_4$ surface also indicate that the EB-evaporated $MgAl_2O_4$ in this study has a cation-disordered spinel structure, which ensures the occurrence of the giant TMR effect, similar to that at a MgO barrier.[2,6]

The largest PMA energy density is obtained for Fe (0.7 nm)/$MgAl_2O_4$ (3 nm) at an annealing temperature of 400 °C. The *M*–*H* loops of this sample are shown in Fig. 2(a), where the effective PMA energy density, that is, $K_{eff}$, was determined from the area enclosed by the in-plane and out-of-plane *M*–*H* loops and the *y* axis (shaded area). The maximum $K_{eff}$ is ~1.0 MJ/m$^3$, which is comparable to the value (~1.4 MJ/m$^3$) in the previous report for an Fe (0.7 nm)/MgO interface. First, it should be noted that the $K_{eff}$ observed in this study is more than twice as large as that reported at an Fe (0.7 nm)/$MgAl_2O_4$ interface (~0.4 MJ/m$^3$),[21] where the $MgAl_2O_4$ was prepared by post-plasma-oxidation of a $Mg_{33}Al_{67}$ metallic layer. Second, the large PMA, which is close to but slightly smaller than that of Fe/MgO, is in good agreement with theoretical predictions.[23] This fact strongly suggests that the first-principles approach describes the mechanism of the interface PMA of an Fe/oxide interface correctly. Theoretical calculations also revealed that the over-

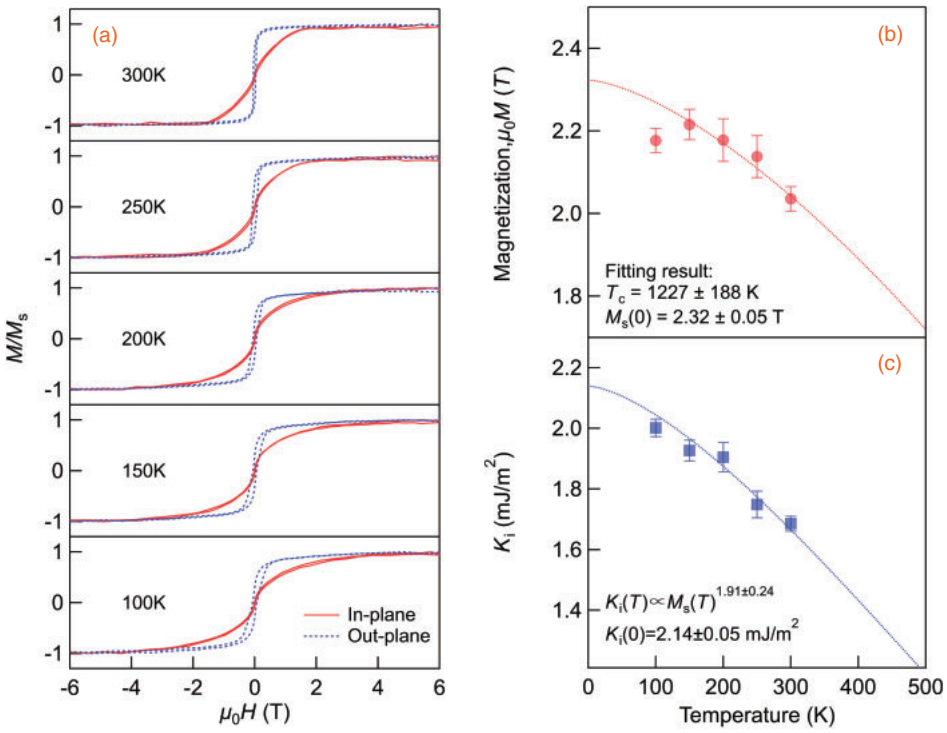


**Fig. 3.** (a) *M*–*H* loops under different measurement temperatures. Measurement temperature dependence of (b) $M_s$ and (c) $K_i$. The dashed lines are results of fitting by Eqs. (1) and (3), respectively.

or underoxidation at the interface of a ferromagnetic layer and an oxide layer significantly reduces the magnitude of the PMA energy density.[14] Thus, EB-evaporated $MgAl_2O_4$ grown from high-density $MgAl_2O_4$ chips may have better interface oxidation conditions than the post-oxidized $MgAl_2O_4$. It was suggested in Ref. 22 that uniform oxidation of a metal layer is not easy, and consequently overoxidation or underoxidation tends to occur at the bottom-side barrier interface depending on the oxidation condition.

By varying the $MgAl_2O_4$ thickness and post-annealing temperature, the interface conditions, such as the degree of oxidation, can be tuned.[19] Figure 2(b) shows $K_{eff}$ as a function of the post-annealing temperature for $t_{MAO} = 2$ and 3 nm. The samples with $t_{MAO} = 3$ nm show a larger PMA energy density than those with $t_{MAO} = 2$ nm at all post-annealing temperatures, which may be related to possible variation of the amount of oxygen near the Fe/$MgAl_2O_4$ interface with increasing $MgAl_2O_4$ thickness. Moreover, the PMA is retained even at 500 °C for $t_{MAO} = 3$ nm, suggesting that the PMA of ultrathin-Fe/$MgAl_2O_4$ is robust enough to tolerate high-temperature heat treatments during industrial manufacturing.[27]

In addition to the magnitude of $K_{eff}$, the weak temperature dependence of $K_{eff}$ is also favorable for practical use of PMA heterostructures. To evaluate the temperature dependence of $K_{eff}$, the *M*–*H* loops of Fe (0.7 nm)/$MgAl_2O_4$ (3 nm) were investigated at different measurement temperatures between 300 K (RT) and 100 K, as shown in Fig. 3(a). It is found that the shape of the in-plane (hard-axis) loops is significantly temperature-dependent. The anisotropy field of the in-plane loops ($H_k$) increases with decreasing temperature, indicating enhancement of $K_{eff}$ at low temperatures. To analyze the temperature dependence of the magnetic properties, we first fitted the saturation magnetization $M_s$ by Bloch's law:[28]

$$M_s(T) = M_s(0)\left[1 - \left(\frac{T}{T_C}\right)^{1.5}\right], \quad (1)$$

where $M_s(0)$ is the $M_s$ value at 0 K, $T$ is the absolute temperature, and $T_C$ is the Curie temperature. The temperature dependence of $M_s$ is plotted in Fig. 3(b) with the fitting curve obtained using Eq. (1). The fitted values of $T_C$ and $M_s(0)$ are 1227 ± 188 K and 2.32 ± 0.05 T, respectively. They are close to the values in bulk Fe, that is, 1043 K and 2.19 T, respectively. Although Bloch's law is not applicable in the temperature range close to $T_C$, the result indicates that the $T_C$ value of Fe in ultrathin-Fe/$MgAl_2O_4$ is not significantly reduced. This contradicts previous reports of ultrathin Fe on Ag[29] or thin Ni and Co on Cu.[30,31] For $K_{eff}$, we assumed the following simple equation:[32]

$$K_{eff} = \frac{K_i}{t_{Fe}} - 2\pi M_s^2 + K_v, \quad (2)$$

where $K_i$, $-2\pi M_s^2$, and $K_v$ are the interface, shape, and volume anisotropy energy densities, respectively. Here, we assumed $K_v = 0$ for simplicity, and $K_i = t_{Fe}(K_{eff} + 2\pi M_s^2)$ is plotted as a function of $T$ in Fig. 3(c). The difference in $K_i$ between 100 and 300 K (~2.0 mJ/m$^2$ at 100 K, ~1.7 mJ/m$^2$ at 300 K) appears to be small compared to that of CoFeB/MgO (~1.9 mJ/m$^2$ at 100 K, ~1.45 mJ/m$^2$ at 300 K),[33] which may be attributed to the high $T_C$ of the Fe layer. Moreover, we fit $K_i$ by a power law of $M_s(T)$:[33]

$$K_i(T) = K_i(0)\left[\frac{M_s(T)}{M_s(0)}\right]^{\gamma}, \quad (3)$$

where $K_i(0)$ is the $K_i$ value at 0 K. The exponent $\gamma = 1.91 \pm 0.24$ obtained by fitting is close to the values reported for CoFeB/MgO (~2.18 and ~2.16).[33,34] Note that according to the Callen–Callen law for uniaxial anisotropy, the exponent

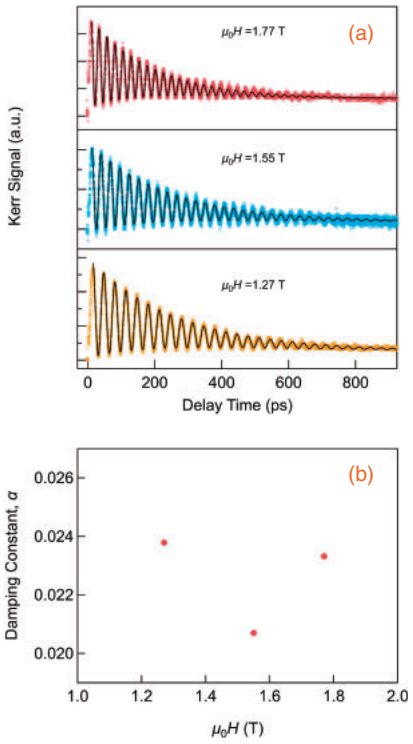


**Fig. 4.** (a) Time-dependent signal (scattered data points) of Fe (0.7 nm)/$MgAl_2O_4$ (3 nm) under external bias magnetic fields ($\mu_0H$) with different strengths and their best fit using Eq. (4) (solid black lines). (b) Calculated effective damping constant $\alpha_{eff}$ as a function of $\mu_0H$.

$\gamma = 3$ is expected; that is, $K(T)/K(0) = [M_s(T)/M_s(0)]^3$, where $K$ is the anisotropy energy.[35] A reduced exponent was theoretically predicted in the presence of large spin–orbit coupling (SOC) materials that contribute to the PMA[36–39] and is consistent with experimental results for FePt.[40] However, further systematic investigation taking into consideration $K_v$ and the higher-order anisotropy is necessary for better understanding.

We also evaluated the damping constant ($\alpha_{eff}$) of the ultrathin Fe layer using the TR-MOKE method, because the damping constants are likely to have positive correlations with the magnitude of the PMA.[41] Such a correlation can be interpreted in light of the fact that both the PMA and magnetic damping originate from spin–orbit interaction. Furthermore, the PMA and magnetic damping can be discussed roughly on the basis of the density of states; small damping constants are expected to be obtained for a system with a small density of states around the Fermi level,[42] whereas a large PMA due to the so-called Bruno mechanism rarely appears.[43] Figure 4(a) shows the oscillatory magnetization precessional signals of the Fe (0.7 nm)/$MgAl_2O_4$ (3 nm) sample with varying $\mu_0H$. $\alpha_{eff}$ is determined by fitting the TR-MOKE signal with a phenomenological fitting function:[44]

$$G(t) = Ae^{-tt_1} + B\sin(2\pi ft - \varphi)e^{-(t/\tau)} + C, \qquad (4)$$

where $f$ is the precessional resonance frequency, $\tau = 1/(2\pi f\alpha_{eff})$ is the relaxation time, and $\varphi$ is the initial phase of oscillation. $A$ and $B$ denote the amplitudes of the oscillations. $C$ and $t_1$ are the offset and decay rate of demagnetization, respectively. We obtained $\alpha_{eff} = 0.0233$, 0.0207, and 0.0238 at $\mu_0H = 1.77$, 1.55, and 1.27 T, respectively, as shown in Fig. 4(b), where the lowest $\alpha_{eff}$ obtained was ~0.0207. Here, $\alpha_{eff}$ is not an intrinsic quantity and indicates only the upper limit of the true $\alpha$ value.[45] It is theoretically predicted that the $\alpha$ value of very thin Fe films, to which the interface effect of Fe contributes most, can be much larger than that of the bulk, although it is unclear at present whether the theoretical prediction is applicable to our experiment.[46] A similar enhancement has also been observed in ultrathin Fe deposited on Ag, where the damping constant for a 0.4 nm Fe film is ~9 times larger than that for thick Fe films.[47]

In summary, we prepared epitaxial ultrathin-Fe/$MgAl_2O_4$ heterostructures by EB evaporation. A large PMA energy density of up to 1.0 MJ/m$^3$ was obtained for an Fe (0.7 nm)/$MgAl_2O_4$ (3 nm) heterostructure annealed at 400 °C, which is in good agreement with theoretical predictions. The PMA was retained even after post-annealing at 500 °C, and the changes in $M_s$ and the PMA energy between 100 and 300 K were relatively small. In addition, the areal PMA energy density $K_i$ was found to be proportional to nearly the square of $M_s$, suggesting that the induced PMA at the Fe/$MgAl_2O_4$ interfaces arises from the strong interface SOC. The lowest effective damping constant was estimated to be 0.0207. This study demonstrated robust interface PMA in ultrathin-Fe/$MgAl_2O_4$, which is useful for p-MTJ applications.

**Acknowledgments** This study was partially supported by the ImPACT program of the Council for Science, Technology and Innovation (Cabinet Office, Government of Japan) and JSPS KAKENHI Grant Number 16H06332. Q.X. acknowledges the National Institute for Materials Science for providing a NIMS Junior Research Assistantship.

1) H. Sukegawa, H. Xiu, T. Ohkubo, T. Furubayashi, T. Niizeki, W. Wang, S. Kasai, S. Mitani, K. Inomata, and K. Hono, Appl. Phys. Lett. **96**, 212505 (2010).
2) H. Sukegawa, Y. Miura, S. Muramoto, S. Mitani, T. Niizeki, T. Ohkubo, K. Abe, M. Shirai, K. Inomata, and K. Hono, Phys. Rev. B **86**, 184401 (2012).
3) S. Yuasa, T. Nagahama, A. Fukushima, Y. Suzuki, and K. Ando, Nat. Mater. **3**, 868 (2004).
4) S. S. P. Parkin, C. Kaiser, A. Panchula, P. M. Rice, B. Hughes, M. Samant, and S.-H. Yang, Nat. Mater. **3**, 862 (2004).
5) Y. Miura, S. Muramoto, K. Abe, and M. Shirai, Phys. Rev. B **86**, 024426 (2012).
6) J. Zhang, X.-G. Zhang, and X. F. Han, Appl. Phys. Lett. **100**, 222401 (2012).
7) T. Scheike, H. Sukegawa, K. Inomata, T. Ohkubo, K. Hono, and S. Mitani, Appl. Phys. Express **9**, 053004 (2016).
8) M. Belmoubarik, H. Sukegawa, T. Ohkubo, S. Mitani, and K. Hono, Appl. Phys. Lett. **108**, 132404 (2016).
9) S. Monso, B. Rodmacq, S. Auffret, G. Casali, F. Fettar, B. Gilles, B. Dieny, and P. Boyer, Appl. Phys. Lett. **80**, 4157 (2002).
10) T. Seki, S. Mitani, K. Yakushiji, and K. Takanashi, Appl. Phys. Lett. **89**, 172504 (2006).
11) A. Manchon, C. Ducruet, L. Lombard, S. Auffret, B. Rodmacq, B. Dieny, S. Pizzini, J. Vogel, V. Uhlíř, M. Hochstrasser, and G. Panaccione, J. Appl. Phys. **104**, 043914 (2008).
12) T. Maruyama, Y. Shiota, T. Nozaki, K. Ohta, N. Toda, M. Mizuguchi, A. A. Tulapurkar, T. Shinjo, M. Shiraishi, S. Mizukami, Y. Ando, and Y. Suzuki, Nat. Nanotechnol. **4**, 158 (2009).
13) S. Ikeda, K. Miura, H. Yamamoto, K. Mizunuma, H. D. Gan, M. Endo, S. Kanai, J. Hayakawa, F. Matsukura, and H. Ohno, Nat. Mater. **9**, 721 (2010).
14) H. X. Yang, M. Chshiev, B. Dieny, J. H. Lee, A. Manchon, and K. H. Shin, Phys. Rev. B **84**, 054401 (2011).
15) W.-G. Wang, M. Li, S. Hageman, and C. L. Chien, Nat. Mater. **11**, 64 (2012).
16) T. Nozaki, K. Yakushiji, S. Tamaru, M. Sekine, R. Matsumoto, M. Konoto, H. Kubota, A. Fukushima, and S. Yuasa, Appl. Phys. Express **6**, 073005 (2013).
17) S. Kanai, Y. Nakatani, M. Yamanouchi, S. Ikeda, H. Sato, F. Matsukura, and H. Ohno, Appl. Phys. Lett. **104**, 212406 (2014).

18) T. Nozaki, A. Kozioł-Rachwał, W. Skowroński, V. Zayets, Y. Shiota, S. Tamaru, H. Kubota, A. Fukushima, S. Yuasa, and Y. Suzuki, Phys. Rev. Appl. **5**, 044006 (2016).
19) Q. Xiang, Z. Wen, H. Sukegawa, S. Kasai, T. Seki, T. Kubota, K. Takanashi, and S. Mitani, J. Phys. D **50**, 40LT04 (2017).
20) J. W. Koo, S. Mitani, T. T. Sasaki, H. Sukegawa, Z. C. Wen, T. Ohkubo, T. Niizeki, K. Inomata, and K. Hono, Appl. Phys. Lett. **103**, 192401 (2013).
21) J. Koo, H. Sukegawa, and S. Mitani, Phys. Status Solidi: Rapid Res. Lett. **8**, 841 (2014).
22) H. Sukegawa, J. P. Hadorn, Z. Wen, T. Ohkubo, S. Mitani, and K. Hono, Appl. Phys. Lett. **110**, 112403 (2017).
23) K. Masuda and Y. Miura, arXiv:1803.10428.
24) K. Lee and S. H. Kang, IEEE Trans. Magn. **46**, 1537 (2010).
25) J.-G. Zhu, Proc. IEEE **96**, 1786 (2008).
26) B. S. Tao, H. X. Yang, Y. L. Zuo, X. Devaux, G. Lengaigne, M. Hehn, D. Lacour, S. Andrieu, M. Chshiev, T. Hauet, F. Montaigne, S. Mangin, X. F. Han, and Y. Lu, Phys. Rev. Lett. **115**, 157204 (2015).
27) Y. Fukumoto, H. Numata, K. Suemitsu, K. Nagahara, N. Ohshima, M. Amano, Y. Asao, H. Hada, H. Yoda, and S. Tahara, Jpn. J. Appl. Phys. **45**, 3829 (2006).
28) N. W. Ashcroft and N. D. Mermin, *Solid State Physics* (Saunders, Philadelphia, PA, 1976).
29) Z. Q. Qiu, J. Pearson, and S. D. Bader, Phys. Rev. Lett. **70**, 1006 (1993).
30) L. H. Tjeng, Y. U. Idzerda, P. Rudolf, F. Sette, and C. T. Chen, J. Magn. Magn. Mater. **109**, 288 (1992).
31) C. M. Schneider, P. Bressler, P. Schuster, J. Kirschner, J. J. de Miguel, and R. Miranda, Phys. Rev. Lett. **64**, 1059 (1990).
32) M. T. Johnson, P. J. H. Bloemen, F. J. A. Den Broeder, and J. J. De Vries, Rep. Prog. Phys. **59**, 1409 (1996).
33) J. G. Alzate, P. Khalili Amiri, G. Yu, P. Upadhyaya, J. A. Katine, J. Langer, B. Ocker, I. N. Krivorotov, and K. L. Wang, Appl. Phys. Lett. **104**, 112410 (2014).
34) A. Okada, S. He, B. Gu, S. Kanai, A. Soumyanarayanan, S. T. Lim, M. Tran, M. Mori, S. Maekawa, F. Matsukura, H. Ohno, and C. Panagopoulos, Proc. Natl. Acad. Sci. U.S.A. **114**, 3815 (2017).
35) H. B. Callen and E. Callen, J. Phys. Chem. Solids **27**, 1271 (1966).
36) J. B. Staunton, S. Ostanin, S. S. A. Razee, B. L. Gyorffy, L. Szunyogh, B. Ginatempo, and E. Bruno, Phys. Rev. Lett. **93**, 257204 (2004).
37) R. Skomski, O. N. Mryasov, J. Zhou, and D. J. Sellmyer, J. Appl. Phys. **99**, 08E916 (2006).
38) J. B. Staunton, L. Szunyogh, A. Buruzs, B. L. Gyorffy, S. Ostanin, and L. Udvardi, Phys. Rev. B **74**, 144411 (2006).
39) Á. Buruzs, P. Weinberger, L. Szunyogh, L. Udvardi, P. I. Chleboun, A. M. Fischer, and J. B. Staunton, Phys. Rev. B **76**, 064417 (2007).
40) S. Okamoto, N. Kikuchi, O. Kitakami, T. Miyazaki, Y. Shimada, and K. Fukamichi, Phys. Rev. B **66**, 024413 (2002).
41) S. Mizukami, S. Iihama, Y. Sasaki, A. Sugihara, R. Ranjbar, and K. Z. Suzuki, J. Appl. Phys. **120**, 142102 (2016).
42) A. Sakuma, J. Phys. D **48**, 164011 (2015).
43) P. Bruno, Phys. Rev. B **39**, 865 (1989).
44) Y. K. Takahashi, Y. Miura, R. Choi, T. Ohkubo, Z. C. Wen, K. Ishioka, R. Mandal, R. Medapalli, H. Sukegawa, S. Mitani, E. E. Fullerton, and K. Hono, Appl. Phys. Lett. **110**, 252409 (2017).
45) S. Mizukami, S. Iihama, N. Inami, T. Hiratsuka, G. Kim, H. Naganuma, M. Oogane, and Y. Ando, Appl. Phys. Lett. **98**, 052501 (2011).
46) E. Barati, M. Cinal, D. M. Edwards, and A. Umerski, Phys. Rev. B **90**, 014420 (2014).
47) B. Heinrich, K. B. Urquhart, A. S. Arrott, J. F. Cochran, K. Myrtle, and S. T. Purcell, Phys. Rev. Lett. **59**, 1756 (1987).